Vol. 28 • No. 11 • March 16 • 2016

www.advmat.de

ADVANCED MATERIALS

WILEY-VCH

Materials Views
www.MaterialsViews.com

ADVANCED MATERIALS
www.advmat.de

COMMUNICATION

Conductive Nanostructured Scaffolds Render Low Local Current Density to Inhibit Lithium Dendrite Growth

*Rui Zhang, Xin-Bing Cheng, Chen-Zi Zhao, Hong-Jie Peng, Jia-Le Shi, Jia-Qi Huang, Jinfu Wang, Fei Wei, and Qiang Zhang**

Reliable and rechargeable batteries with a high specific energy are vital for a wide variety of applications in portable, transportable, and stationary energy storage applications. Lithium metal-based batteries (LMBs) (Li–sulfur (Li–S) and Li–air (Li–O_2) batteries) have received considerable attention,[1] because Li metal can store 10 times more energy than graphite. Actually, the Li metal anode is strongly considered as the "Holy Grail" of rechargeable batteries due to the extremely high theoretical specific capacity (3860 mA h g^{-1}) and the lowest negative electrochemical potential (−3.040 V vs the standard hydrogen electrode).[2,3] However, the practical applications of rechargeable LMBs are hindered by two issues all induced by inhomogeneous and uncontrolled Li deposition, that is, Li dendrites. The first one is the safety concern. The growth of Li dendrites in continuous cycles may render internal short circuit and further incur fire. The other issue is the low cycling efficiency ascribed to the unstable solid electrolyte interphase (SEI), which is generated from the immediate reactions of the Li metal and electrolyte and is even exaggerated by the large contact surface induced by dendrite growth. As the Li dendrites form and disappear repeatedly, the SEI undergoes continuous regeneration upon exposed fresh Li, consuming large amount of Li and therefore leading to low efficiency. "Dead Li" caused by the inhomogeneous dissolution of Li dendrites aggravates the further loss of available Li metal.[4] Therefore, inhibiting the uncontrolled growth of Li dendrites during the repeated Li depositing/stripping process is critically essential towards the full utilization of Li metal anode.

The dendritic growth of Li metal has been investigated since the 1960s and the research in Li metal anode has never come to a standstill during the past 40 years.[3,5] Several approaches have been proposed to settle the dendrite issue through (1) liquid electrolyte modification (lithium bis(fluorosulfonyl)imide (LiFSI),[6,7] LiF,[8] H_2O,[9] $LiNO_3$, polysulfide,[10,11] Cs^+,[12] fluoroethylene carbonate,[13] and concentrated electrolyte[14]), (2) polymer and solid electrolyte (liquid-like solid electrolyte,[15] $Li_7P_2S_8I$,[16] cross-linked polyethylene/poly(ethylene oxide) electrolytes,[17] single-ion polymer[18]), and (3) artificial SEI (hollow carbon nanospheres,[19] Li_3N protection layer or PEDOT-co-PEG coating layer,[20] composite protective layer (CPL),[21] ceramic layers,[22] LISICON film[23]), etc. These achievements afford novel insight and mechanistic understanding into the growth behavior and structure regulation of Li dendrites.[24] Although it is well known that many factors (such as local current density, elastic strength of SEI layer, ionic/electron diffusion coefficient, etc.) have significant impacts on the formation and growth of Li dendrites, a clear understanding on their impact mechanism is still lacked. The widely accepted diffusion model (Equation (1)) is proposed to correlate the "Sand's time τ" with the transfer nature of Li^+ ions and electrons empirically as follows[25]

$$\tau = \pi D \frac{eC_0\left(\mu_a + \mu_{Li^+}\right)^2}{2J\mu_a} \tag{1}$$

where τ is the time when Li dendrites start to grow, D is the diffusion coefficient. e is the electronic charge. C_0 is the initial concentration of Li salt. μ_a and μ_{Li^+} are the anionic and Li^+ mobility, respectively. J is the effective electrode current density. The SEI layer can affect the μ_{Li^+} to act a role on the Sand's time (τ). The transport of electrons can affect the effective electrode current density (J) of the electrode, and thus plays a role on the Sand's time (τ). The smaller effective electrode current density (J) and larger Li^+ mobility induce larger Sand's time (τ), which indicates that the cell has long lifespan before the growth of Li dendrites. Therefore, Sand's time model can relate the nature of SEI layer and electrode structure to the dendrite growth.

As shown in Equation (1), current density is a crucial factor to regulate the morphology of Li deposits. The dendrite growth can be inhibited in each cell system when the local current density is much reduced. Consequently, many attempts have been explored to reduce the local current density of the Li depositing sites on the promise of the large bulk current density to guarantee the rapid charging rate of batteries. The nanowires and a pomegranate-inspired hierarchical nanostructure have been successfully fabricated with micro/nanoscale size, which have proved to be effective in silicon anode to relieve the large volume changes.[26] Bieker and co-workers introduced Li metal anode based on coated Li powder.[27] Compared to flat Li foil, the coated 50 µm Li powder anode can relatively suppress the dendrite formation, as the local current density during depositing/stripping was reduced due to the increased surface area. Aiming at reducing the characteristic dimension of the electrode to nanoscale, Li_7B_6 fiber was proposed with the diameter of ≈200 nm, which rendered the dendrite-free morphology and demonstrated a superior cycling performance in high-energy-density Li–S batteries.[28]

R. Zhang, X.-B. Cheng, C.-Z. Zhao, H.-J. Peng,
J.-L. Shi, Prof. J.-Q. Huang, Prof. J. F. Wang,
Prof. F. Wei, Prof. Q. Zhang
Beijing Key Laboratory of Green Chemical
Reaction Engineering and Technology
Department of Chemical Engineering
Tsinghua University
Beijing 100084, China
E-mail: zhang-qiang@mails.tsinghua.edu.cn

DOI: 10.1002/adma.201504117

To reduce the matrix size further and improve the conductivity, 3D-reduced graphene oxide (rGO) was also employed as the framework of Li deposits in a Li_2S_8–$LiNO_3$–lithium bis(trifluoromethanesulfonyl)imide (LiTFSI) electrolyte.[29] The synergy between the Li_2S_8 and $LiNO_3$ in the ether-based electrolyte has been well understood by Cui and co-workers. A robust SEI was built on the Li anode,[10] which is an important contribution to efficient use of Li metal in a rechargeable battery. However, these advanced matrices (e.g., rGO, Li_7B_6 fiber, Li power) are still with relatively low specific surface area (SSA) and would not decrease the local current density sufficiently to reliable value for very fast charging. These structures are also with a low electrical conductivity, resulting in a large electrical resistance and strong polarization at high current rates. Consequently, if an intrinsic conductive scaffold with a very high SSA (>1000 m^2 g^{-1}) and superior electrical conductivity (>100 S cm^{-1}) can be employed as the matrix for Li deposition, the local current density is expected to be significantly reduced and the dendrite growth will be suppressed in the composite anode.

Here, an unstacked graphene framework with deposited Li metal was proposed to be a high-efficiency and stable Li metal anode in a LiTFSI–LiFSI dual-salt ether based electrolyte. The unstacked graphene employed herein was a 3D hexagonal "drum" with only two layers and exhibited a very large SSA (1666 m^2 g^{-1}), pore volume (1.65 cm^3 g^{-1}), and electrical conductivity (435 S cm^{-1}) (Figure S1, Supporting Information). Such unstacked graphene with huge SSA provides the feasibility to demonstrate the proof-of-concept of the regulation of Li depositing morphology through the ultralow local areal current density in LMBs. The LiTFSI–LiFSI dual-salt electrolyte that formed protective SEI layer and proved effectiveness in increasing the Coulombic efficiency of LMBs (the ratio of Li stripping capacity to Li depositing capacity)[6,7] was firstly applied in nanostructured metal anode to protect the Li deposits in the graphene matrix.

The depositing/stripping behaviors of graphene-based LMBs are schematically illustrated in **Figure 1**. Due to the ultralow local current density, Li ions migrated through the SEI and deposited homogeneously on the graphene "drum" during the charging process, forming a sandwich-like core–shell structure, which was with the core of graphene, the outer shell of Li and the outermost shell of SEI. The sandwich-like structure not only inhibited the nucleation and growth of Li dendrite due to the ultralow local current density, but also improved the Coulombic efficiency by blocking the electrolyte out of the shell. When Li metal lost the electrons during the discharging process, the deposited Li striped from the interspace of the graphene and SEI, leaving the similar sandwich-like SEI-covering-graphene structure. Consequently, the unique structure of graphene-based Li metal anode maintained the stable cycling of LMBs with dendrite-free morphology and high Coulombic efficiency.

The morphology of Li deposits on graphene-based anode cycled in dual-salt electrolyte at an electrode current density of 0.5 mA cm^{-2} (1.0 mA cm^{-2} = 1333 mA g^{-1}) is exhibited in **Figure 2**. There were a great number of pores supported by unstacked graphene "drum" (Figure 2a) that was obtained from CH_4 through hard template growth on calcined layered double hydroxides (LDHs).[30] The flakes were hexagonal with a uniform lateral size of ≈3 µm (Figure 2b). Densely distributed protuberances which supported the unstacked layers with the interlayer spacing of ≈10 nm extending from the graphene sheets were found (indicated by the arrows shown in the inset of Figure 2b). The short carbon nanotube protuberances guaranteed the unstacking morphology of graphene "drum" with extremely high SSA and pore volume.[30] After 2.0 mA h cm^{-2} (1.0 mA h cm^{-2} = 1333 mA h g^{-1}) Li deposition on the graphene-based anode, SEI layer covered the graphene, as well as Li metal deposited into the interspace of SEI and graphene without arising of Li dendrites. The surface of charged Li metal anode was smooth (Figure 2c), indicating a dendrite-free deposition. There were several small Li deposition bumps with the size of ≈50–100 nm on the surface of one graphene flake (Figure 2d). The deposition bumps with tens of nanometers were the evidence of ultralow current density, which will be illustrated in the following section.

After Li stripped from the interspace of graphene and SEI, SEI layer remained well to encase the graphene flakes, and the pores built by unstacked graphene flakes before cycling reemerged (Figure 2e). A great number of concave areas arose on the SEI layer with the approximately similar size of ≈50–100 nm as the bumps in Figure 2d on graphene flakes (Figure 2f), which induced by the dissolution of bump-like deposited lithium, indicating the unique depositing/stripping morphology at such ultralow local current density. The sandwich-like core–shell structure with SEI covering graphene flakes were observed clearly with the thickness of SEI layer of around 30 nm after Li stripping (the inset in Figure 2f). Consequently, the graphene-based Li metal anode demonstrated

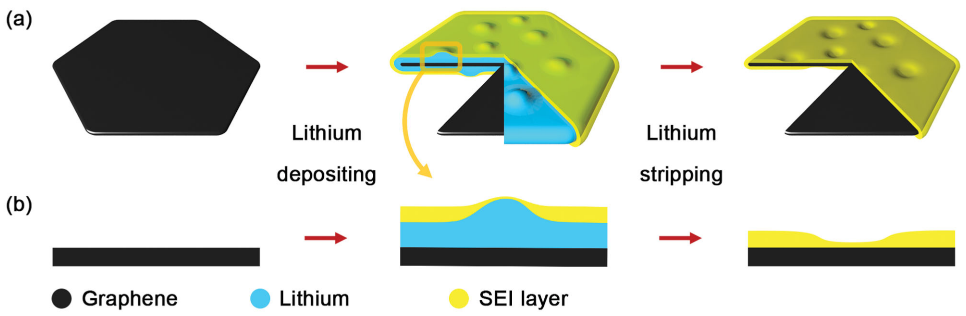

Figure 1. Schematic diagrams of Li depositing/stripping process on one graphene flake. The diagrams before cycles, after Li depositing, after Li stripping of a) one graphene flake and b) its sectional view. Li (blue) deposited/striped without dendrites under the protection of flexible SEI layer (yellow) on graphene flake (black).

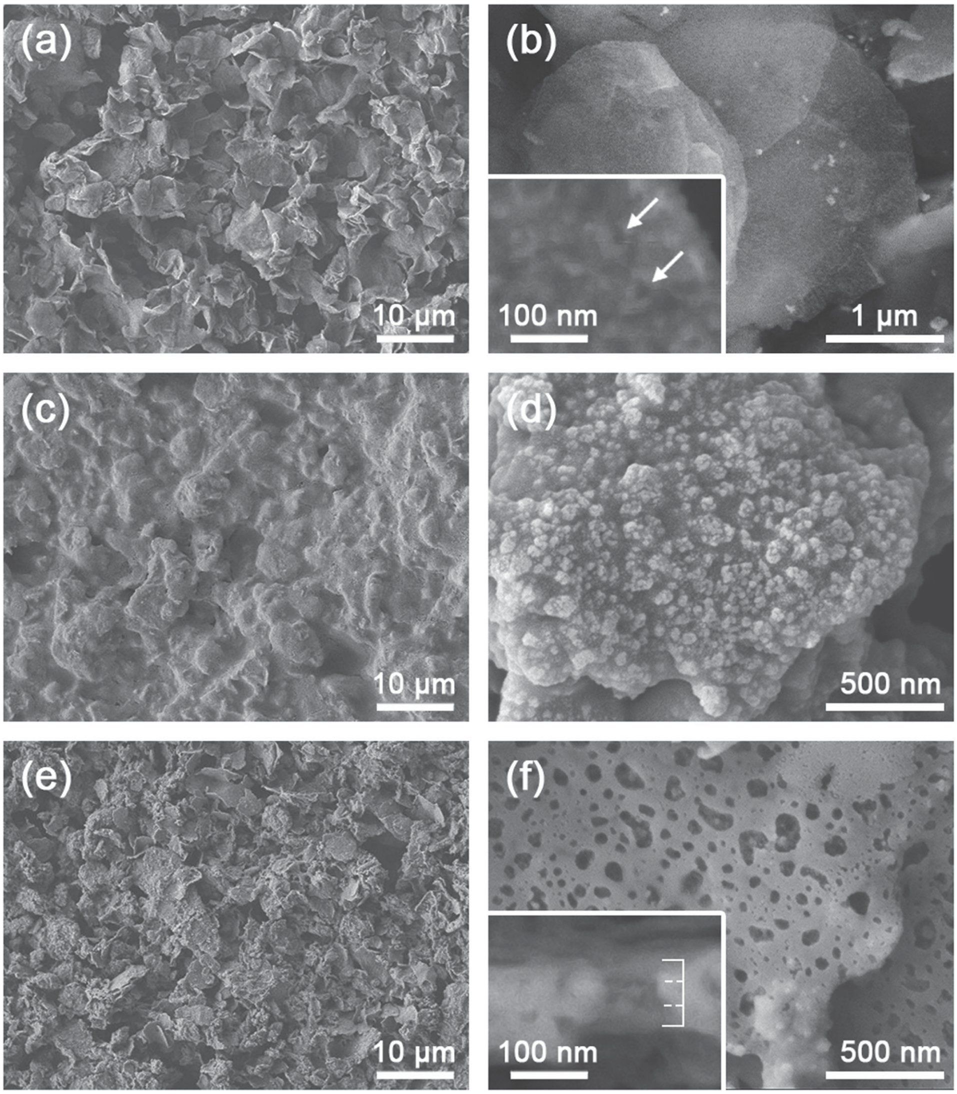

Figure 2. Morphology characterization of graphene-based anode at a current density of 0.5 mA cm^{-2}. SEM images of graphene-based anode: a, b) before cycles, c, d) after Li depositing, and e, f) after Li stripping. Inset in (b) is a high resolution SEM image of pores on one graphene flake. Inset in (f) is the side view of one graphene flake, showing the sandwich-like SEI-covering-graphene structure.

a dendrite-free morphology after Li depositing and a stable SEI layer after Li stripping. Even after 10 cycles, the SEI-graphene and lithiated SEI–Li–graphene structure can be well preserved (Figure S2, Supporting Information).

A quantitative model was proposed to confirm the critical role of the ultralow local current density on the Li depositing morphology. As the graphene synthesized herein was with a large SSA of 1666 m^2 g^{-1} and an areal loading amount of 0.75 mg cm^{-2} on Cu foil, the local surface area provided by graphene on the anode was 1.2 m^2 per 1.0 cm^{-2} (Cu foil). Consequently, when the cell was cycled at a current density of 0.5 mA $cm_{Cu\ foil}^{-2}$, the local current density of Li depositing sites on graphene-based anodes was around 4.0×10^{-5} mA cm_g^{-2}, ten thousandth of that on routine Cu foil-based anode.

To verify the role of the ultralow local current density, a controlled electrochemical test was conducted by charging a Cu foil-based anode (graphene-free) at a current density of 4.0×10^{-5} mA $cm_{Cu\ foil}^{-2}$ with a lithiation capacity of 1.6×10^{-4} mA h cm^{-2} (the same as the local lithiation capacity on the local surface on graphene-based anode). Several small Li deposition bumps with a size of ≈50–100 nm were observed on the surface of Cu foil-based anode at the ultralow current density (**Figure 3**a), which was consistent with that on one graphene flake with a local current density of 4.0×10^{-5} mA cm_g^{-2} (corresponding to 0.5 mA $cm_{Cu\ foil}^{-2}$) (Figure 3b).

However, when the current density of Cu foil-based anode was increased to 0.5 mA $cm_{Cu\ foil}^{-2}$, there was a large quantity of Li dendrites with a length of ≈10 μm on the surface of Cu foil (Figure 3c,d). Consequently, the ultralow local current density was efficient and effective to inhibit dendrite growth. The unstacked graphene "drum" reported herein with the large SSA and superior electrical conductivity realized the proof-of-concept of the role of current density on the morphology of Li deposits.

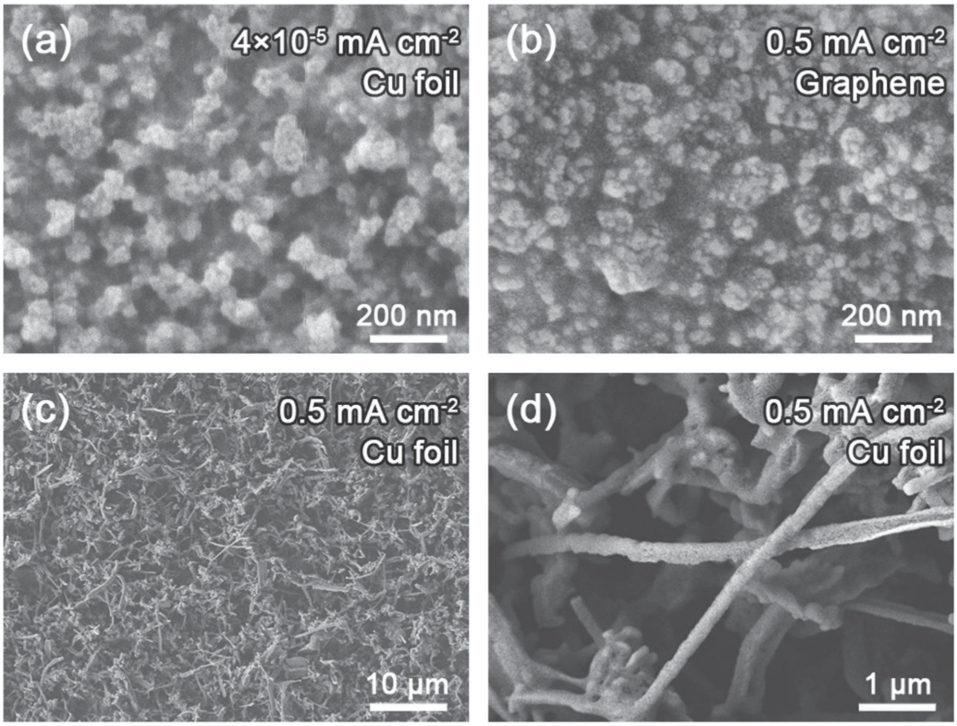

Figure 3. SEM images of Li deposits at different current densities. a) Li depositing morphology on Cu foil-based anode at an ultralow current density of 4×10^{-5} mA cm^{-2}. b) Li depositing morphology on graphene-based anode at a current density of 0.5 mA cm^{-2}. c, d) Li dendrites on Cu foil-based anode at an increased current density of 0.5 mA cm^{-2}.

The dendrite-free morphology after Li depositing and the SEI-graphene structure after Li stripping required a stable, flexible, and compact SEI layer with high elastic modulus. The graphene-induced Li deposits were always with small sizes, which were easy to be consumed by the electrolyte if the SEI layer was not stable and compact enough to protect the Li metal, leading to the low Coulombic efficiency (Figure S3, Supporting Information). To enhance the lithiation capacity of the graphene-based anode, SEI layer should be with strong flexibility, ensuring that the SEI layer was levitated off graphene flakes when Li depositing and landed onto graphene flakes completely when Li stripping. Therefore, the SEI layer in the dual-salt electrolyte was just like the head of a drum. While pounding the drum, the drumhead sank and while stopping the pounding, the drumhead bulged again and the drumhead preserved well.

The protective SEI layer was built by the reaction of LiTFSI–LiFSI dual-salt electrolyte and Li metal. It is reported that compared to widely used LiTFSI in 1,3-dioxolane (DOL)/1,2-dimethoxyethane (DME) electrolyte, the LiTFSI–LiFSI dual-salt electrolyte could form better protective SEI layer due to the increased LiF content.[7,8] X-ray photoelectron spectroscopy (XPS) test was carried out to reveal the surface chemistry of the SEI layer in dual-salt electrolyte and LiTFSI in DOL/DME electrolyte (Figure S4, Supporting Information). The inorganic components in the SEI layer mainly included LiF, Li_2CO_3, etc. LiF salt was considered to be very remarkable in forming stable and compact SEI layer.[7,8] From the F 1s spectra in Figure S4, there was a significant increase in LiF component. The organic components in the SEI layer mainly included RCH_2OLi, CH_3OCO_2Li, CH_3CO_2Li, etc. Some of the oligomers generated from LiFSI or DME in the surface of SEI layer could also enhance the stability and flexibility of SEI layer.[7,31] After Li plating, the SEI layer can maintain stable in the composition (Figure S4c, Supporting Information). The LiFSI component in dual-salt electrolyte not only provides high conductivity, but also dominates the interfacial behavior, inducing a much thinner and dense inorganic layer containing LiF in SEI layer, while LiTFSI in DOL solvent acts as stabilizer and conducting agent.[7] With the employing of such LiTFSI–LiFSI in DOL/DME dual-salt electrolyte, a protective SEI layer was formed in our unstacked graphene-based anode.

Coulombic efficiency is a formidably important parameter to evaluate the sustainability of the specific anode for LMBs. The two-electrode cells (Li vs graphene-based anode or Cu foil-based anode) were assembled to characterize the efficiency of graphene-based anode. At the electrode current density of 0.5 mA cm^{-2} for a cycling capacity of 0.5 mA h cm^{-2}, the Coulombic efficiency of graphene anode could reach ≈93%, while that of Cu foil anode vibrated from 65% to 85% during cycles, demonstrating the advantage of graphene-based anode in Coulombic efficiency with high stability and utilization (**Figure 4**a). It should be noted that the high Coulombic efficiency was achieved after several initial cycles in which the stable SEI layer was formed. The pretreatment of the cells carried out here in Li metal battery is a universal convention in Li–ion battery fabrication. During the pretreatment of the anode, a local capacity of nearly 7.2×10^{-5} mA h cm^{-2} was consumed to form the stable SEI layer for the graphene-based anode. However, the consumed Li on the Cu foil surface was 1.1 mA h cm^{-2} during

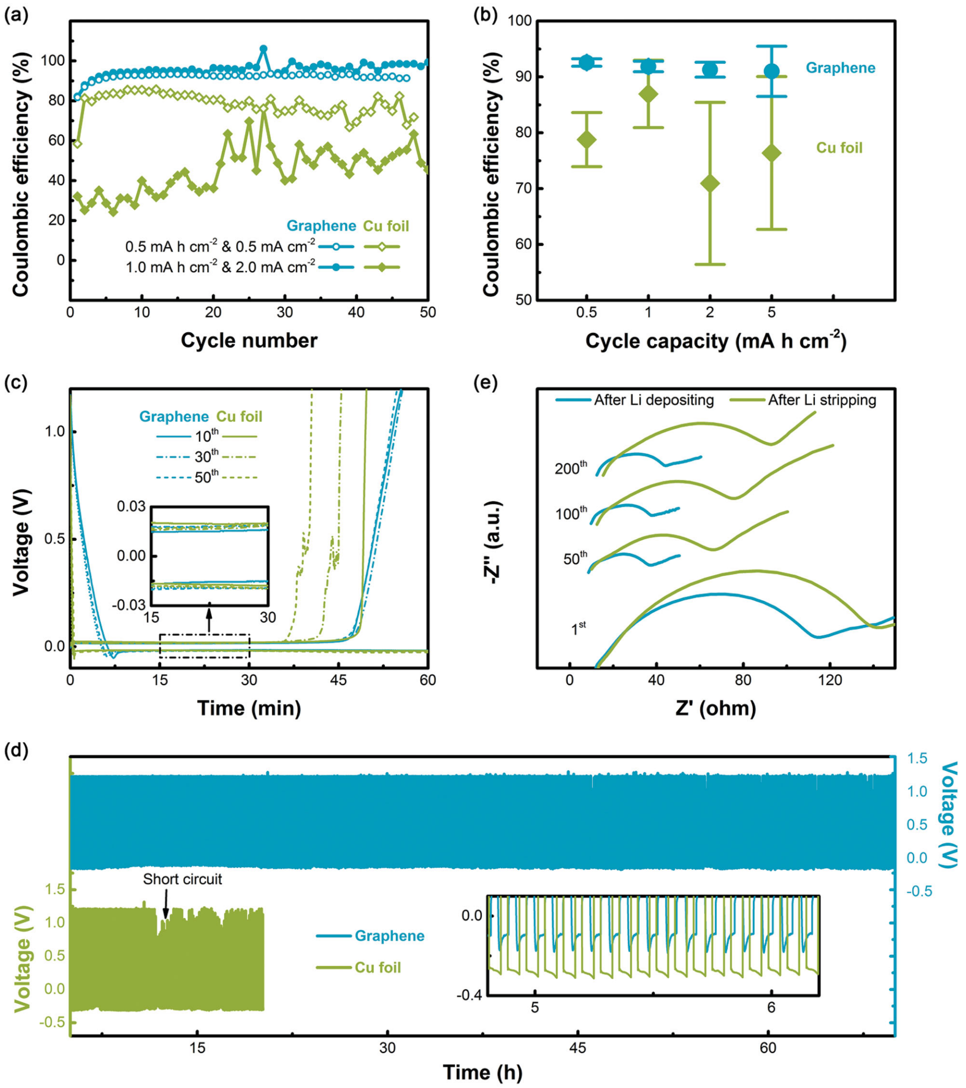

Figure 4. Electrochemical characterization of graphene-based anode. a) The Coulombic efficiency of graphene- and Cu foil-based anode with a cycling capacity of 0.5 mA h cm^{-2} at a current density of 0.5 mA cm^{-2} and a cycling capacity of 1.0 mA h cm^{-2} at a higher current density of 2.0 mA cm^{-2}. b) Average Coulombic efficiency and its variance in the cycles of graphene- and Cu foil-based anode with different cycling capacities at 0.5 mA cm^{-2}. c) Voltage profiles of the 10th, 30th, and 50th cycle of graphene- and Cu foil-based anode with a cycling capacity of 0.5 mA h cm^{-2} at 0.5 mA cm^{-2}. d) Voltage–time curves in 800 cycles of graphene- and Cu foil-based anode with a cycling capacity of 0.1 mA h cm^{-2} at 2.0 mA cm^{-2}. e) Impedance spectroscopy of graphene-based anode after Li stripping and depositing in (d). Inset in (c) is an expanded view of the bottom plot. Inset in (d) is an expanded view of the voltage–time curves at the time from 5 to 6 h.

the SEI-forming cycles, which was much larger than that of graphene-based anode. More importantly, the SEI layer on the Cu foil surface was not stable and continuously consumed Li metal in the following cycles, thus rendering the large impedance and short cycling life of cells.

When the current density was increased to 2.0 mA cm^{-2}, the graphene-based anode also exhibited impressive performance of Coulombic efficiency. The graphene-based anode could cycle with the nearly same Coulombic efficiency with that of cells cycling at 0.5 mA cm^{-2}, which was much higher than that of Cu foil-based anode (Figure 4a). The superior high rate performance was ascribed to the high SSA and electrical conductivity of unstacked graphene, providing the possibility of fast charging capability for LMBs.

The flexible SEI layer on the graphene-based anode renders the cell with a high lithiation capacity. When the cycling capacity was increased to 1.0, 2.0, and 5.0 mA h cm^{-2}, similar results were achieved for the graphene-based anode (Figure 4b). At 0.5, 1.0, 2.0, and 5.0 mA h cm^{-2}, the fluctuations in Coulombic efficiency were 6.2%, 6.9%, 20%, and 18% for Cu foil-based anode, respectively, while they were just 0.72%, 1.0%, 1.5%, and 4.9% for graphene-based anode. The superior high-capacity performance for graphene was ascribed to the high pore volume (1.65 cm^3 g^{-1}) that contributed by the huge number of pores on unstacked graphene flakes. It is calculated that unstacked graphene with such a large pore volume renders a high theoretical Li cycling capacity of 4.0 mA h mg$_g^{-1}$. The relative large fluctuation in Coulombic efficiency for graphene-based anode can be attributed to the fact that the higher cycling capacity (5.0 mA h cm^{-2}) just exceeded over the theoretical capacity (3.0 mA h cm^{-2} or 4.0 mA h mg$_g^{-1}$) of graphene-based anode. The overloaded Li deposition inducing extra volume change made negative effect on Coulombic efficiency performance, from which reflects the importance of a large pore volume in nanostructured Li metal anode.

The voltage profiles in Figure 4c exhibit stable depositing/stripping behaviors for graphene-based anode with a hysteresis of 15 mV. While for Cu foil-based anode, there was obvious capacity decay in the 10th, 30th, and 50th cycles. The large irreversible Li deposits on the Cu foil-based anode resulted in the loss of Li metal and may form a thick and insulating layer on the Cu foil, leading to terminate the service life of cycling cells.[4]

To investigate the long-cycle performance of graphene-based anode at a high current rate, an 800-cycle systematic test was conducted with a depositing/stripping capacity of 0.1 mA h cm^{-2} at 2.0 mA cm^{-2}. Stable voltage profiles of graphene-based anode were found during the 800 cycles (Figure 4d). The hysteresis of Li depositing/stripping for the modified electrode (≈150 mV) was much smaller than that of Cu foil-based anode (≈300 mV), indicating a rapid Li–ion transfer through SEI to deposit onto or strip from graphene flakes.

The stability of interfacial transporting behavior was explored by electrochemical impedance spectroscopy (EIS), which was a nondestructive, convenient, and powerful technique for testing and diagnosing SEI (Figure 4e). Except for the initial cycle, the impedance after Li depositing and stripping was very low and stable in the whole cycling life of the cell in Figure 4d. It was noted that the interface impedance (referring to the semicircle in higher frequency of EIS) after Li depositing was always much smaller than that after Li stripping, which was possibly due to the thinner and smoother SEI layer with higher ionic conductivity after fully Li depositing than that after fully Li stripping. The high Coulombic efficiency, low diffusion impedance, and stable cycling performance confirmed the vital roles of graphene and induced ultralow local current density in the LMBs.

The unstacked graphene-based nanostructured Li metal anode in this contribution exhibits impressive performance on both dendrite inhibition and electrochemical behavior, which we consider mainly benefit from the synergistic effect of ultralow local current density and the stable SEI layer from the dual-salt electrolyte. On the one hand, the ultralow local current density regulated by high SSA inhibits the initial nucleation of Li dendrites, and renders uniform dendrite-free morphology, but the introduction of nanostructure without strong protection may enhance the surface reactions between Li and electrolyte. On the other hand, the stable SEI layer induced by dual-salt electrolyte acts as the strong protection layer mentioned above, which inhibits further reactions between deposited Li and electrolyte. This cooperation finally affords high cycling efficiency and brings superior performance. As a result, both ideal nanostructures and protective SEI layers are highly required for a robust Li metal anode.

According to the electrochemical depositing/stripping of Li ions on/from the metal anode, the ideal nanostructure in the composite anode should possess (1) high SSA that guarantees ultralow local current density and then inhibits dendrite nucleation due to the Sand's model; (2) appropriately high pore volume, which provides enough space for protective SEI layer and cyclic Li deposition; (3) relatively smooth surface to inhibit tip dendrites nucleation; (4) high electrical conductivity; (5) excellent structural stability; as well as (6) superior electrochemical stability. The corresponding expected protective SEI layer should exhibit (1) high flexibility to adapt ultrahigh volume change during Li depositing/stripping process; (2) high compactness to fully cover Li layer and inhibit further reactions between Li and electrolyte; (3) high elastic strength to suppress dendrites growth; (4) high Li$^+$ ionic conductivity; and (5) ultralow electric conductivity.

Graphene materials have been extensively explored due to its extraordinary electronic and mechanical properties. The advantages of high SSA and electronic conductivity render the wide application of graphene materials in the field of battery energy storage systems, especially the resuscitative Li metal anode. Jang and co-workers employed graphene as the electrode of the Li metal anode.[32] However, the high power graphene-Li/graphene cell was with a cycling capacity of less than 200 mA h g^{-1}, which significantly sacrificed the advantage of high-energy-density LMBs. To improve the energy density of graphene-based Li metal anode, Koratkar and co-workers obtained free-standing porous graphene networks as high-capacity anode with the capacity of 900 mA h g^{-1}.[33] The improved capacity was attributed to the predominance of Li_3C_8 and lithium metal plating as the primary and favorable reaction mechanisms. Choi and co-workers reported multilayered graphene (MLG) coating Li metal anode with Cs$^+$ additive to further enhance the energy density of Li metal anode.[34] MLG protected SEI formation from Li dendrites and thus stabilized Coulombic efficiency in each cycle. 3D graphene foam was also applied as the framework of Li deposits in a Li_2S_8–$LiNO_3$–LiTFSI electrolyte.[29] Graphene with high SSA was very effective to inhibit the dendrite growth. However, because of the facile stacking of graphene sheets induced by the huge surface area and strong π–π interactions, reduced graphene oxide is always with small SSA of less than 300 m^2 g^{-1}. The unstacked graphene "drum" employed herein provided much lower current density, higher cycle capacity, and better lithium depositing/stripping morphology due to its much higher SSA (1666 m^2 g^{-1}), higher pore volume (1.65 cm^3 g^{-1}), higher electrical conductivity (435 S cm^{-1}), and better structural stability. Besides, the introduction of dual-salt electrolyte enhances the protection of SEI layer in its flexibility, compactness, and stability. Such $LiNO_3$-free electrolyte is not oxidative and is expected to be employed at harsh working condition. However, there is still a large gap to the ideal nanostructured Li metal anode, especially to the ideal protective SEI layer. Much more exploration is highly required to explore and synthesize ideal nanostructures and protective SEI layers.

In summary, we have constructed a distinctive nanostructured Li metal anode entrapped in unstacked graphene "drum". The graphene-induced ultralow local current density indicated a superior performance in inhibiting Li dendrite growth. Coupling with the LiTFSI–LiFSI dual-salt electrolyte, graphene-based anode maintained a stable, flexible, and compact SEI layer, which led to a high Coulombic efficiency of 93% at a high lithiation capacity of 5.0 mA h cm^{-2} and a high current density of 2.0 mA cm^{-2}, as well as a stable depositing/stripping morphology in the 800-cycle service life. The ultralow local current density effectively serving Li metal anode can shed a new light on dendrite issues of other metal anode (such as Na, Mg, Zn, etc.) and the overcharging issues of Li–ion batteries. Future research is required to further improve the Li depositing/stripping morphology and electrochemical performance by designing preferable anode structure and producing more protective SEI layer. It is also desperately required to investigate the diffusion behavior of Li ions and electrons in the process of Li depositing and stripping to advance the commercial applications of Li metal-based and other metal-based batteries by the synergism of electrochemical mechanism and efficient material design.

Experimental Section

Materials: The Li metal counter electrode was purchased from China Energy Lithium Co., Ltd. The anhydrous DOL and anhydrous DME were purchased from Zhuhai Smoothway Electronic Material Co., Ltd. LiTFSI was purchased from Alfa Aesar. LiFSI was purchased from Suzhou Fluolyte Co., Ltd.

Synthesis of Unstacked Graphene: Firstly, a urea assisted co-precipitation reaction was employed to prepare the hexagonal MgAl–LDH template precursors with a lateral size of ≈3.0 μm. Then the graphene was prepared by CH_4-chemical vapor deposition growth with calcined LDHs as the templates in a horizontal quartz tube reactor. The reactor was quickly heated to 950 °C and maintained there for 10 min under flowing Ar (200 mL min^{-1}). Afterwards, CH_4 (800 mL min^{-1}) was introduced into the reactor for graphene deposition. The reaction was maintained for 10 min before the furnace was cooled to room temperature under Ar protection. The as-grown raw products were purified by NaOH (15.0 M) aqueous solution at 180 °C for 12.0 h and HCl (5.0 M) aqueous solution at 80 °C for 12.0 h sequentially to remove the MgAl-layered double oxide (LDO) flakes. After filtering, washing, and freeze-drying, the unstacked double-layer templated graphene were finally obtained. The yield of unstacked graphene on MgAl-layered double oxide was ≈0.12 $g_{graphene}$ g_{LDO}^{-1}.

Characterization: N_2 isotherms of graphene were obtained at −196 °C (77 K) with an Autosorb-IQ$_2$-MP-C system (Quantachrome, USA). The SSA was determined by the Brunauer–Emmett–Teller method. The pore size distributions were calculated using the density functional theory method from the adsorption branches of the isotherms. Both SEM (JSM 7401F, JEOL Ltd., Japan) operated at 3.0 kV and a TEM (JEM 2100, JEOL Ltd., Japan) operated at 120.0 kV were employed to characterize the morphology of Li deposition on graphene anode and Cu foil anode. The metal sample was protected with Ar during transfer process. An XPS (ESCALAB 250Xi, Thermo Fisher Scientific Inc., USA) was employed to analyze the chemical components of SEI layer generated in dual-salt electrolyte.

Electrochemical Measurement: Two-electrode symmetrical cells using standard CR2025 coin-type cells and STC24 dismountable cells (Shenzhen Kejingstar Technology Ltd.) were employed. The two-electrode symmetrical cells were assembled in an Ar-filled glove box with O_2 and H_2O content below 1 ppm. Graphene powder and polyvinylidene fluoride binder (PVDF) (mass ratio of graphene:PVDF = 85:15) were mixed into a slurry by magnetic stirring in *N*-methylpyrrolidone for ≈24.0 h. The slurry with a thickness of 150 μm was coated onto a Cu foil and dried in a vacuum drying oven at 60 °C for 6.0 h, and the thickness of the dried coated graphene was measured to be 30 μm by SEM image (Figure S5, Supporting Information). The as-obtained foil was punched into disks with a diameter of 13.0 mm as the working electrode. 1.0 mm thick Li metal foil was employed as the counter electrode. LiTFSI–LiFSI dual-salt electrolyte of 80 μL was added as the electrolyte in each cell. The dual-salt electrolyte in this work was prepared by mixing electrolyte I (0.75 M LiTFSI in DOL) and electrolyte II (1.5 M LiFSI in DME) in 2:1 (volume ratio). The coin cells were monitored in galvanostatic mode within a voltage range of −0.5 to 1.2 V using Neware multichannel battery testing system (Neware Technology Ltd., China). In each galvanostatic cycle, the charge time was fixed in the lithium depositing process, but the discharge time in the lithium stripping process was only controlled by a cut-off voltage at 1.2 V without time limit. The electrochemical impedance spectroscopy measurement and the ultralow current density charging test on Cu foil-based anode were performed on Solartron 1470E electrochemical workstation (Solartron Analytical, UK).

Supporting Information

Supporting Information is available from the Wiley Online Library or from the author.

Acknowledgements

R.Z., X.-B.C. contributed equally to this work. This work was supported by the Natural Scientific Foundation of China (21422604 and 21561130151), National Basic Research Program of China (2015CB932500), and Tsinghua University Initiative Scientific Research Program (20141081231 and 2014z22076).

Received: August 23, 2015
Revised: November 5, 2015

[1] a) L. Grande, E. Paillard, J. Hassoun, J.-B. Park, Y.-J. Lee, Y.-K. Sun, S. Passerini, B. Scrosati, *Adv. Mater.* **2015**, *27*, 784; b) Y. Lu, M. Tikekar, R. Mohanty, K. Hendrickson, L. Ma, L. A. Archer, *Adv. Energy Mater.* **2015**, *5*, 1402073; c) X.-B. Cheng, R. Zhang, C.-Z. Zhao, F. Wei, J.-G. Zhang, Q. Zhang, *Adv. Sci.* **2016**, *3*, 1500213.
[2] W. Xu, J. L. Wang, F. Ding, X. L. Chen, E. Nasybutin, Y. H. Zhang, J. G. Zhang, *Energy Environ. Sci.* **2014**, *7*, 513.
[3] X.-B. Cheng, Q. Zhang, *J. Mater. Chem. A* **2015**, *3*, 7207.
[4] D. Lv, Y. Shao, T. Lozano, W. D. Bennett, G. L. Graff, B. Polzin, J. Zhang, M. H. Engelhard, N. T. Saenz, W. A. Henderson, P. Bhattacharya, J. Liu, J. Xiao, *Adv. Energy Mater.* **2015**, *5*, 1400993.
[5] a) J. L. Wang, F. J. Lin, H. Jia, J. Yang, C. W. Monroe, Y. N. NuLi, *Angew. Chem. Int. Ed.* **2014**, *53*, 10099; b) H. J. Peng, T. Z. Hou, Q. Zhang, J. Q. Huang, X. B. Cheng, M. Q. Guo, Z. Yuan, L. Y. He, F. Wei, *Adv. Mater. Interfaces* **2014**, *1*, 1400227; c) R. Mukherjee, A. V. Thomas, D. Datta, E. Singh, J. Li, O. Eksik, V. B. Shenoy, N. Koratkar, *Nat. Commun.* **2014**, *5*, 3710; d) L. M. Suo, Y. S. Hu, H. Li, M. Armand, L. Q. Chen, *Nat. Commun.* **2013**, *4*, 1481; e) M. S. Whittingham, *Proc. IEEE.* **2012**, *100*, 1518; f) H.-J. Peng, J. Liang, L. Zhu, J.-Q. Huang, X.-B. Cheng, X. Guo, W. Ding, W. Zhu, Q. Zhang, *ACS Nano* **2014**, *8*, 11280; g) A. Manthiram, Y. Fu, S.-H. Chung, C. Zu, Y.-S. Su, *Chem. Rev.* **2014**, *114*, 11751.
[6] J. J. Hu, G. K. Long, S. Liu, G. R. Li, X. P. Gao, *Chem. Commun.* **2014**, *50*, 14647.
[7] R. R. Miao, J. Yang, X. J. Feng, H. Jia, J. L. Wang, Y. N. Nuli, *J. Power Sources* **2014**, *271*, 291.
[8] Y. Y. Lu, Z. Y. Tu, L. A. Archer, *Nat. Mater.* **2014**, *13*, 961.
[9] J. Qian, W. Xu, P. Bhattacharya, M. Engelhard, W. A. Henderson, Y. Zhang, J.-G. Zhang, *Nano Energy* **2015**, *15*, 135.
[10] W. Li, H. Yao, K. Yan, G. Zheng, Z. Liang, Y.-M. Chiang, Y. Cui, *Nat. Commun.* **2015**, *6*, 7436.
[11] S. Xiong, K. Xie, Y. Diao, X. Hong, *J. Power Sources* **2014**, *246*, 840.

[12] a) F. Ding, W. Xu, G. L. Graff, J. Zhang, M. L. Sushko, X. L. Chen, Y. Y. Shao, M. H. Engelhard, Z. M. Nie, J. Xiao, X. J. Liu, P. V. Sushko, J. Liu, J. G. Zhang, *J. Am. Chem. Soc.* **2013**, *135*, 4450; b) Y. Zhang, J. Qian, W. Xu, S. M. Russell, X. Chen, E. Nasybulin, P. Bhattacharya, M. H. Engelhard, D. Mei, R. Cao, F. Ding, A. V. Cresce, K. Xu, J.-G. Zhang, *Nano Lett.* **2014**, *14*, 6889.

[13] Q.-C. Liu, J.-J. Xu, S. Yuan, Z.-W. Chang, D. Xu, Y.-B. Yin, L. Li, H.-X. Zhong, Y.-S. Jiang, J.-M. Yan, X.-B. Zhang, *Adv. Mater.* **2015**, *27*, 5241.

[14] a) J. Qian, W. A. Henderson, W. Xu, P. Bhattacharya, M. Engelhard, O. Borodin, J.-G. Zhang, *Nat. Commun.* **2015**, *6*, 6362; b) L. Suo, Y.-S. Hu, H. Li, M. Armand, L. Chen, *Nat. Commun.* **2013**, *4*, 1481.

[15] J. Zhang, Y. Bai, X.-G. Sun, Y. Li, B. Guo, J. Chen, G. M. Veith, D. K. Hensley, M. P. Paranthaman, J. B. Goodenough, S. Dai, *Nano Lett.* **2015**, *15*, 3398.

[16] E. Rangasamy, Z. Liu, M. Gobet, K. Pilar, G. Sahu, W. Zhou, H. Wu, S. Greenbaum, C. Liang, *J. Am. Chem. Soc.* **2015**, *137*, 1384.

[17] R. Khurana, J. L. Schaefer, L. A. Archer, G. W. Coates, *J. Am. Chem. Soc.* **2014**, *136*, 7395.

[18] R. Bouchet, S. Maria, R. Meziane, A. Aboulaich, L. Lienafa, J.-P. Bonnet, T. N. T. Phan, D. Bertin, D. Gigmes, D. Devaux, R. Denoyel, M. Armand, *Nat. Mater.* **2013**, *12*, 452.

[19] G. Y. Zheng, S. W. Lee, Z. Liang, H. W. Lee, K. Yan, H. B. Yao, H. T. Wang, W. Y. Li, S. Chu, Y. Cui, *Nat. Nanotechnol.* **2014**, *9*, 618.

[20] a) G. Ma, Z. Wen, M. Wu, C. Shen, Q. Wang, J. Jin, X. Wu, *Chem. Commun.* **2014**, *50*, 14209; b) G. Ma, Z. Wen, Q. Wang, C. Shen, J. Jin, X. Wu, *J. Mater. Chem. A* **2014**, *2*, 19355; c) Y. J. Zhang, W. Wang, H. Tang, W. Q. Bai, X. Ge, X. L. Wang, C. D. Gu, J. P. Tu, *J. Power Sources* **2015**, *277*, 304.

[21] H. Lee, D. J. Lee, Y.-J. Kim, J.-K. Park, H.-T. Kim, *J. Power Sources* **2015**, *284*, 103.

[22] a) K.-i. Chung, W.-S. Kim, Y.-K. Choi, *J. Electroanal. Chem.* **2004**, *566*, 263; b) G. A. Umeda, E. Menke, M. Richard, K. L. Stamm, F. Wudl, B. Dunn, *J. Mater. Chem.* **2011**, *21*, 1593.

[23] Y. F. Hao, M. S. Bharathi, L. Wang, Y. Y. Liu, H. Chen, S. Nie, X. H. Wang, H. Chou, C. Tan, B. Fallahazad, H. Ramanarayan, C. W. Magnuson, E. Tutuc, B. I. Yakobson, K. F. McCarty, Y. W. Zhang, P. Kim, J. Hone, L. Colombo, R. S. Ruoff, *Science* **2013**, *342*, 720.

[24] J. L. Schaefer, D. A. Yanga, L. A. Archer, *Chem. Mater.* **2013**, *25*, 834.

[25] a) V. Fleury, J. N. Chazalviel, M. Rosso, B. Sapoval, *J. Electroanal. Chem. Interfacial Electrochem.* **1990**, *290*, 249; b) J. N. Chazalviel, *Phys. Rev. A* **1990**, *42*, 7355; c) C. Brissot, M. Rosso, J. N. Chazalviel, P. Baudry, S. Lascaud, *Electrochim. Acta* **1998**, *43*, 1569; d) M. Rosso, T. Gobron, C. Brissot, J. N. Chazalviel, S. Lascaud, *J. Power Sources* **2001**, *97–98*, 804.

[26] a) C. K. Chan, H. Peng, G. Liu, K. McIlwrath, X. F. Zhang, R. A. Huggins, Y. Cui, *Nat. Nanotechnol.* **2008**, *3*, 31; b) N. Liu, Z. Lu, J. Zhao, M. T. McDowell, H.-W. Lee, W. Zhao, Y. Cui, *Nat. Nanotechnol.* **2014**, *9*, 187.

[27] J. Heine, S. Krüger, C. Hartnig, U. Wietelmann, M. Winter, P. Bieker, *Adv. Energy Mater.* **2014**, *4*, 130081.

[28] a) X. B. Cheng, H. J. Peng, J. Q. Huang, F. Wei, Q. Zhang, *Small* **2014**, *10*, 4257; b) X. Zhang, W. Wang, A. Wang, Y. Huang, K. Yuan, Z. Yu, J. Qiu, Y. Yang, *J. Mater. Chem. A* **2014**, *2*, 11660.

[29] X.-B. Cheng, H.-J. Peng, J.-Q. Huang, R. Zhang, C.-Z. Zhao, Q. Zhang, *ACS Nano* **2015**, *9*, 6373.

[30] M. Q. Zhao, Q. Zhang, J. Q. Huang, G. L. Tian, J. Q. Nie, H. J. Peng, F. Wei, *Nat. Commun.* **2014**, *5*, 3410.

[31] H. Kim, F. Wu, J. T. Lee, N. Nitta, H.-T. Lin, M. Oschatz, W. I. Cho, S. Kaskel, O. Borodin, G. Yushin, *Adv. Energy Mater.* **2015**, *5*, 1401792.

[32] A. Zhamu, G. Chen, C. Liu, D. Neff, Q. Fang, Z. Yu, W. Xiong, Y. Wang, X. Wang, B. Z. Jang, *Energy Environ. Sci.* **2012**, *5*, 5701.

[33] R. Mukherjee, A. V. Thomas, D. Datta, E. Singh, J. Li, O. Eksik, V. B. Shenoy, N. Koratkar, *Nat. Commun.* **2014**, *5*, 3710.

[34] J.-S. Kim, D. W. Kim, H. T. Jung, J. W. Choi, *Chem. Mater.* **2015**, *27*, 2780.